Volume 2 | Number 8 | August 2018

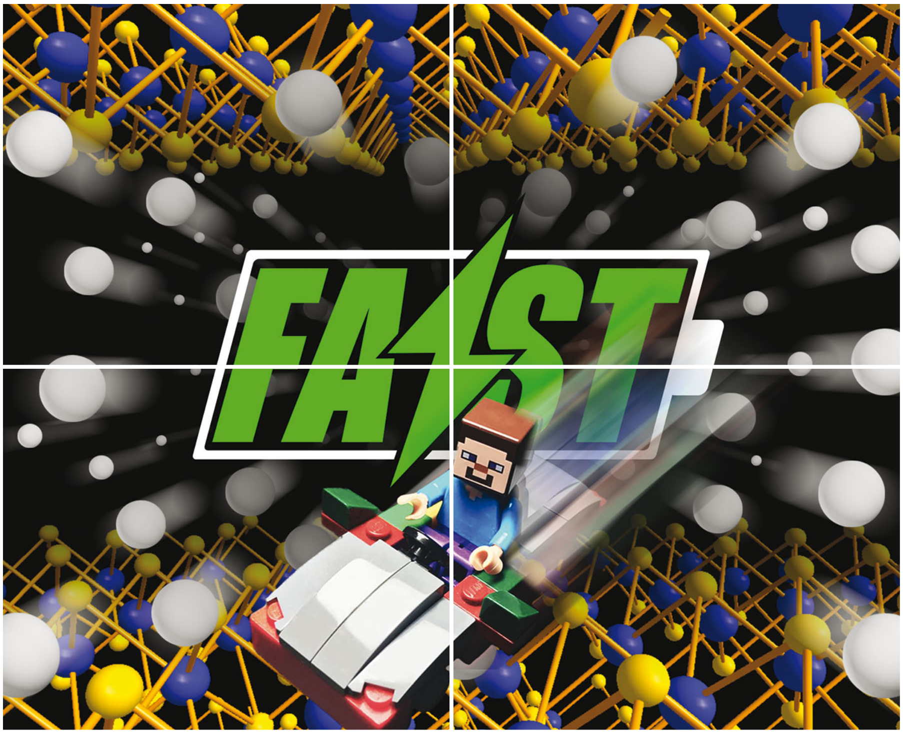

MATERIALS CHEMISTRY FRONTIERS

中国化学会
Chinese Chemical Society
ICCAS
ROYAL SOCIETY OF CHEMISTRY
rsc.li/frontiers-materials

MATERIALS CHEMISTRY
FRONTIERS

RESEARCH ARTICLE

View Article Online
View Journal | View Issue

Cite this: *Mater. Chem. Front.*, 2018, **2**, 1441

Directionally assembled MoS_2 with significantly expanded interlayer spacing: a superior anode material for high-rate lithium-ion batteries†

Qilin Wei,‡[a] Min-Rui Gao, ‡[b] Yan Li,‡[c] Dongtang Zhang,[a] Siyu Wu, [a] Zonghai Chen[c] and Yugang Sun *[a]

Received 19th March 2018,
Accepted 16th April 2018

DOI: 10.1039/c8qm00117k

rsc.li/frontiers-materials

Despite the great promise of molybdenum disulfide (MoS_2) as a storage anode for rechargeable lithium-ion batteries, the corresponding rate capacity is limited by the low electrical conductivity and kinetic barriers linked to ion diffusion, which prevents MoS_2 from being used in current electrical energy storage devices. A feasible strategy is reported to tackle these challenges by directionally growing MoS_2 nanosheets with an expanded interlayer spacing (*i.e.*, 9.4 Å *versus* 6.15 Å for pristine 2H-MoS_2) on multiwalled carbon nanotubes (MWCNTs), which is performed through the microwave-assisted solvothermal reduction of ammonium tetrathiomolybdate [$(NH_4)_2MoS_4$] in dimethylformamide in the presence of MWCNTs. The intimate interfaces between the MoS_2 edges and the MWCNTs as well as the expanded interlayer gaps in MoS_2 offer efficient and rapid pathways for ion and electron transport, which is favorable for improving the performance of batteries and enables the highest rate capability to be achieved. Batteries containing the as-synthesized MoS_2/MWCNT anodes can constantly deliver a reversible capacity of 390 mA h g^{-1} at a current rate of up to 57.312 A g^{-1} (36C), describing the first class of MoS_2-based anodes promising for high-rate use.

1. Introduction

Rechargeable lithium-ion batteries (LIBs) have been widely adopted for powering portable electronics, while current technologies remain inadequate for applications such as hybrid or electric vehicles, and electric transportation, in which high rate capability is required. Ideal electrode materials for these emerging applications should possess fast ion and electron transport kinetics in addition to high specific capacity, hence improving the energy storage at high charge/discharge rates. Common strategies explored to enhance ion and electron transport in active electrode materials include using nanostructures, which offer exceptionally short transport lengths and significantly reduced lithium ion diffusion time, and hybridizing them with electrically conductive additives such as carbon.[1–3] Besides, for layered intercalation hosts, expanding the interlayer distance could also effectively improve the intrinsic ion diffusivity, owing to the decreased diffusion energy barrier, which has been verified theoretically[4–6] and experimentally.[5,7–10] However, no significant improvements in rate performance have been observed for the studied layer-structured materials.

Recently, transition metal dichalcogenides with layered structures have aroused a lot of interest from the viewpoints of their versatile physics and chemistry as well as natural abundance.[11–14] Among these materials, molybdenum disulfide (MoS_2) is fundamentally and technologically interesting for a wide variety of applications including electrochemical energy storage,[15–17] catalysis,[18] chemical sensing,[19,20] transistors,[21] and photodetectors,[22] due to its unique electronic/optoelectronic properties.[11,12,15,18,19,21,22] The use of MoS_2 as lithium ion storage electrode of LIBs is highly promising as it presents considerable advantages in terms of high rate capability, high capacity retention, small volumetric expansion and low cost.[23] MoS_2 crystallizes in a graphite-like lamellar structure that is coupled by weak van der Waals forces and readily allows ion intercalation chemistry. Considerable effort has been invested for the development of MoS_2 for lithium storage, typically focused on synthesizing highly nanostructured materials to shorten the diffusion path for ions and electrons,[8,24–28] and on combining MoS_2 with carbon materials to increase its electrical conductivity.[29–33] Other strategies for this purpose include introducing dipole molecules (*e.g.*, water) to reduce the polarization of solvated ions,

---

[a] *Department of Chemistry, Temple University, 1901 North 13th Street, Philadelphia, Pennsylvania 19122, USA. E-mail: ygsun@temple.edu*
[b] *Center for Nanoscale Materials, Argonne National Laboratory, 9700 South Cass Avenue, Argonne, Illinois 60439, USA*
[c] *Chemical Sciences and Engineering Division, Argonne National Laboratory, 9700 South Cass Avenue, Argonne, Illinois 60439, USA*

† Electronic supplementary information (ESI) available. See DOI: 10.1039/c8qm00117k

‡ These authors contributed equally.

thereby boosting the ion diffusivity,[5] or incorporating a suitable polymer such as poly-(ethylene oxide) (PEO) that possesses ion coordination properties to accelerate lithium ion transportation.[34] Nevertheless, using MoS_2-based materials as candidate electrodes for rapid charging and discharging is still not yet realized.[8]

In this article, a new class of anode material is reported, consisting of interlayer-expanded MoS_2 nanosheets directionally anchored on multiwalled carbon nanotubes (denoted as IE-MoS_2/MWCNTs), which enables high specific capacity, excellent capacity retention, satisfactory coulombic efficiency, and especially good rate capability. It exhibits a reversible charge/discharge capacity of 1442 mA h g^{-1} at 1.592 A g^{-1} (1C) and retains excellent capacity with a small polarization at a rate as high as 57.3 A g^{-1} (36C). The successful synthesis benefits from the rational promotion of the heterogeneous nucleation of MoS_2 on the controlled oxidized MWCNTs through the microwave-assisted solvothermal reduction of $(NH_4)_2MoS_4$ in dimethylformamide (DMF). Because of the simplicity, low energy consumption, and ease in scaling up, the method developed for synthesizing IE-MoS_2/MWCNTs offers new opportunities for the rational design of electrode materials with enhanced conductivity and rate performances.

2. Experimental section

2.1 Chemical oxidation of MWCNTs

All chemicals were used as received without further purification. The controlled oxidation of MWCNTs was carried out according to the process reported elsewhere.[35] In brief, 0.3 g of MWCNT powder was dispersed in a 25 mL aqueous solution formed by mixing sulphuric acid (H_2SO_4, 96 wt%) and hydrogen peroxide (H_2O_2, 30 wt%) ($V_{H_2SO_4} : V_{H_2O_2} = 7:3$) in a 100 mL round-bottom flask equipped with a condenser. The dispersion was constantly stirred for 5 h to completely disperse the MWCNTs. The resulting dispersion was then diluted with an appropriate amount of water, followed by filtration. The collected black solid was washed with water thoroughly until the pH of the washing water became neutral. The washed solid was then placed in a fume hood and dried for 2 days in the ambient environment. The dry solid was re-dispersed in DMF (anhydrous, 99.8%, Sigma-Aldrich) to form a dispersion with a concentration of ∼3 mg mL^{-1}.

2.2 Synthesis of IE-MoS_2/MWCNTs

In a typical synthesis, 10 mg of $(NH_4)_2MoS_4$ (99.97%, Sigma-Aldrich) was added to 6 mL of a DMF dispersion of oxidized MWCNTs, followed by vigorous magnetic stirring for 15 min under ambient conditions. The resulting solution was transferred into a 10 mL microwave reaction vessel, which was sealed and heated to 240 °C at a fast temperature ramp in a Monowave 300 microwave reactor (Anton Paar). The solution temperature was maintained for an appropriate time. The reaction solution was then cooled down to room temperature with pressurized nitrogen flow. The synthesized IE-MoS_2/MWCNT product was collected *via* centrifugation at 6000 r.p.m. (revolutions per minute) for 5 min. After the removal of the colourless supernatant, the precipitate was washed with distilled water and absolute ethanol at least 4 times, followed by drying at 60 °C in an oven for 4 h. Elemental analysis indicated that the MoS_2 loading in the IE-MoS_2/MWCNT composite was 36 wt%. Since the DMF solution of $(NH_4)_2MoS_4$ exhibited a brown colour, the colourless supernatant indicated that the synthesis yield reached approximately 100%.

2.3 Characterization

The as-synthesized samples were examined by X-ray diffraction (XRD), which was carried out on a Bruker D2 Phaser X-ray diffractometer with Cu Kα radiation (λ = 1.5406 Å) at 30 kV and a current of 10 mA. TEM and HRTEM images were recorded on a JEOL 2010F(s) transmission electron microscope operated at an acceleration voltage of 200 kV. The energy dispersive X-ray (EDX) spectra were collected with an INCA X-ray microanalysis system equipped on the JEOL 2010F(s) microscope. All the samples were prepared by drop-casting the ethanol suspensions of interesting nanostructures onto carbon-coated copper grids, followed by drying in a fume hood at room temperature. The synchrotron small-angle X-ray scattering (SAXS) measurement was performed at the beam line 12-ID-B of the Advanced Photon Source (APS), Argonne National Laboratory.

2.4 Battery assembly and performance evaluation

In a typical process for fabricating working electrodes with the synthesized IE-MoS_2/MWCNTs, 850 mg of IE-MoS_2/MWCNTs was mixed with *N*-methyl-2-pyrrolidone (NMP, Sigma-Aldrich), 50 mg of C45 (Timcal), and 100 mg of polyvinylidene (PVdF, Kureha KF-9300) to form a slurry. This slurry was then coated on Cu foil (60 cm × 70 cm) using a doctor blade, followed by drying in a vacuum oven set at 75 °C overnight to evaporate the NMP solvent. The loading of the IE-MoS_2/MWCNTs for the electrode was ∼0.2 mg cm^{-2}. Punching the film formed electrode discs with a size of 0.5 cm in diameter, which were then further dried under vacuum at 110 °C to remove any moisture trapped in the electrode. The 2032-type coin cells were assembled in an argon-filled glove box (O_2, H_2O <5 ppm) using the as-fabricated electrode discs as anodes and lithium foils as the counter electrodes (cathode). The electrodes were separated with a Celgard 2325 separator soaked with an electrolyte (Tomiyama Chemical Industry, Japan) consisting of 1.2 M $LiPF_6$ in ethylene carbonate (EC) : ethyl methyl carbonate (EMC) with a weight ratio of 3 : 7. Anodes made of pure IE-MoS_2 nanostructures and MWCNTs were also fabricated and used to assemble coin cells by following the same procedure.

The assembled coin cells were all cycled on a Maccor cycler. They first went through an initial activation step at room temperature, which consisted of three cycles between 3 V and 0.0005 V with C/20 current. Then, the cells were aged within the same voltage range but with 1C rate to evaluate their cycling performance. The specific capacities were calculated based on the mass of the integrated IE-MoS_2/MWCNTs including the mass of both MoS_2 and MWCNTs. After either activation step or targeted 1C aged cycles, the cells were discharged to 0.9 V and held at that potential for more than 15 hours to wait for the AC impedance measurement. An EG&G 273A potentiostat and a

Solartron SI1260 frequency response analyzer controlled by the ZPLOT measurement software were used. The impedance spectra were collected between 100 kHz and 10 mHz, with a 10 mV perturbation around the open-circuit voltage.

3. Results and discussion

3.1 Characterization of the IE-MoS_2/MWCNT heterostructures

The IE-MoS_2/MWCNT hybrid structures are prepared by microwave-heating a DMF solution of $(NH_4)_2MoS_4$ in the presence of MWCNTs under solvothermal conditions. Fig. 1 highlights the major steps involved in the synthesis and the structure of the product. It is noteworthy that pure MWCNTs usually present poor wettability with foreign active materials. The MWCNTs are firstly oxidized with a mixture of H_2SO_4 (96 wt%) and H_2O_2 (30 wt%) to provide oxygen-containing groups[35] that exhibit increased wettability towards the Mo precursor. The enhanced affinity promotes the heterogeneous nucleation of MoS_2 upon reduction of MoS_4^{2-} ions at high temperatures, leading to the formation of MoS_2/MWCNT hybrid structures. Due to the increased reducing ability of DMF at elevated temperatures, the oxidized MWCNTs (Ox-MWCNTs) are reduced to MWCNTs by eliminating the oxygen-containing groups. The chemical conversion of the Ox-MWCNTs to MWCNTs stops the continuous nucleation of MoS_2 on the Ox-MWCNTs. Therefore, the continuous reduction of MoS_4^{2-} ions only grow the existing MoS_2 nuclei into larger MoS_2 nanosheets. The non-wettability between MoS_2 and MWCNTs (*i.e.*, hydrophilic MoS_2 *versus* hydrophobic MWCNTs) forces the growing MoS_2 nanosheets to protrude out of the MWCNT surfaces, enabling a directional assembly of the as-grown MoS_2 nanosheets on the outermost walls of the MWCNTs with the formation of intimate interfaces between the MoS_2 edges and MWCNT walls. Such a directionally aligned growth of the MoS_2 nanosheets on the MWCNTs has also been observed in the synthesis of MoS_2/graphene composites.[36,37] Similar to the synthesis in the absence of MWCNTs, the resulting MoS_2 nanosheets on the MWCNTs also exhibit an expanded interlayer spacing of 9.4 Å (*versus* 6.15 Å for pristine 2H-MoS_2).[38] The large interlayer gap is mostly ascribed to the leftover species (*e.g.*, DMF solvent molecules or NH_4^+ ions) of the synthesis reaction.

Fig. 2 presents a typical sample of IE-MoS_2/MWCNTs synthesized from a reaction performed at 240 °C for 100 min. The corresponding transmission electron microscopy (TEM) images (Fig. 2a–c) show the sheet-like MoS_2 grown uniformly around each MWCNT. Each MoS_2 nanosheet consists of only a few (3–5) S–Mo–S molecular layers and it links to the MWCNT through its edge rather than its basal surface. Most MoS_2 nanosheets exhibit sizes less than 20 nm. Control experiments illustrate that using the MWCNTs without oxidation treatment leads to the failure of anchoring MoS_2 (Fig. S1, ESI†); while in the absence of the MWCNTs, the exact same synthesis produces sphere-like assemblies of the MoS_2 nanosheets, where homogeneous nucleation takes place (Fig. S2, ESI†). Independent from the nucleation process, such microwave chemistry always forms nanostructured MoS_2 with an enlarged interlayer spacing of 9.4 Å, which is consistent with the high-resolution TEM (HRTEM) image as shown in Fig. 2c.

Fig. 2d shows the X-ray diffraction (XRD) pattern of the synthesized IE-MoS_2/MWCNT product, in which the strong Bragg peak at 25.8° corresponds to the (002) reflections of the MWCNTs with a lattice spacing of 3.4 Å.[39] The wide-angle reflections in a 2θ range of 30°–70° can be indexed to the hexagonal MoS_2 (JCPDS 77-1716). The asymmetric nature of the reflections indicates the turbostratic feature of the grafted MoS_2 nanosheets, presumably

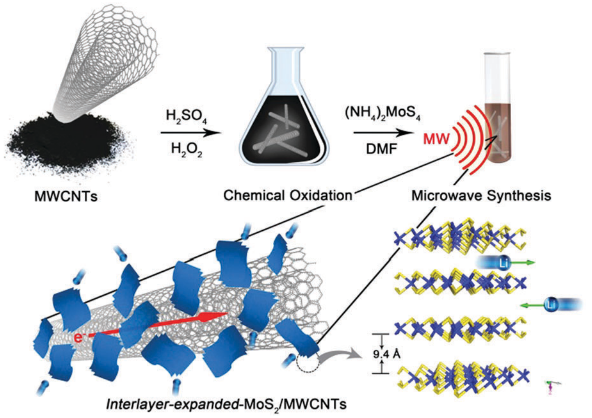

Fig. 1 Schematic illustration of the synthesis of the IE-MoS_2/MWCNTs through a microwave-assisted solvothermal reduction of $(NH_4)_2MoS_4$ in DMF in the presence of oxidized MWCNTs. The resulting MoS_2 nanosheets exhibit an expanded interlayer spacing of 9.4 Å and directionally anchor on the outermost walls of the MWCNTs, forming interfaces between the MoS_2 edges and the MWCNT walls.

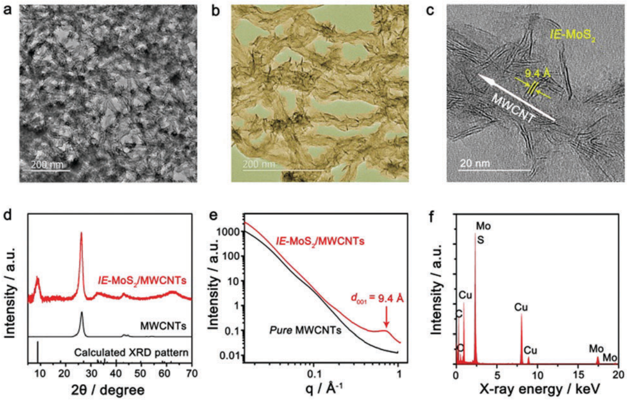

Fig. 2 Characterization of the synthesized IE-MoS_2/MWCNT hybrid structures. (a and b) Typical TEM images with different magnifications. (c) HRTEM image of a partial MWCNT decorated with IE-MoS_2 nanosheets, showing characteristic features including thin thickness of the MoS_2 nanosheets, an expanded MoS_2 interlayer spacing of 9.4 Å, and interfaces between the MoS_2 edges and the MWCNT wall. (d) Comparison of the XRD patterns of the IE-MoS_2/MWCNTs (red) and MWCNTs (black), revealing the formation of MoS_2 with an expanded interlayer spacing and the intactness of the MWCNTs in the course of the synthesis illustrated in Fig. 1. The sticks represent the theoretical peak positions and their relative intensities corresponding to MoS_2 with an expanded interlayer spacing of 9.4 Å. (e) Comparison of synchrotron SAXS patterns of the IE-MoS_2/MWCNTs (red) and the corresponding MWCNTs (black). (f) EDX spectrum of the IE-MoS_2/MWCNTs.

caused by, for example, the presence of stacking faults among S–Mo–S molecular layers as a result of *a–b* plane gliding.[38,40] The symmetric peak at a low angle of 9.4° originates from the (002) reflections of the layer-structured MoS_2 with an interlayer spacing of 9.4 Å, which is consistent with the HRTEM observation. Such an expanded interlayer spacing is also confirmed with the synchrotron small-angle X-ray scattering (SAXS) pattern, which displays a single scattering peak centered at $q = 0.67$ Å^{-1} (corresponding to 9.4 Å in d spacing determined from $q = 2\pi/d$) (Fig. 2e). In contrast, the corresponding MWCNTs do not show any characteristic SAXS peaks, further confirming the interlayer-expanded feature of the MoS_2 nanosheets. Compared to the d spacing of 6.15 Å for pristine 2H-MoS_2, about 53% expansion of the S–Mo–S interlayer distance is observed in the synthesized IE-MoS_2/MWCNTs, which may facilitate the intercalation/diffusion of lithium ions.[4,5] The energy-dispersive X-ray (EDX) spectrum (Fig. 2f) identifies Mo, S, and C as the major elemental components (Cu and part of the C signals emanating from the carbon-coated TEM grid), further demonstrating the formation of IE-MoS_2/MWCNT hybrid structures.

3.2 Electrochemical performance of the IE-MoS_2/MWCNT heterostructures

Lithium ion storage performance in the as-synthesized IE-MoS_2/MWCNTs of Fig. 2 has been evaluated in 2032-type coin cells using lithium metal as the counter electrode. Each cell is initially discharged at a low rate of C/20 (20 h) to activate the electrode material along with storing lithium ions in IE-MoS_2 (activation process). Fig. 3a presents cyclic voltammograms (CVs) of an IE-MoS_2/MWCNT electrode conducted at a slow scan rate of 0.5 mV s^{-1}. Two cathodic peaks at 0.99 and 0.45 V in the initial cycle can be attributed to lithium intercalation into the layered MoS_2, leading to a possible transition from the trigonal prismatic 2H semiconducting phase to the octahedral 1T metallic phase (Fig. S3, ESI†),[41,42] followed by a conversion reaction and eventually a deep conversion to a stoichiometrically equivalent Mo- and Li_2S-rich composition, which is still a derivative of reduced MoS_2 containing Li^+ (*e.g.*, Li_3MoS_2).[29,32,42] The peakless current variation between 0.99 and 0.45 V is ascribed to the continuous insertion of lithium ions into the expanded MoS_2 interlayer gaps in the course of discharge.[43,44] The following anodic process shows two lithium extraction peaks at 1.76 and 2.29 V, which are related to the oxidation of intermediate conversion species (*e.g.*, Li_3MoS_2 containing possible Mo and Li_2S clusters, $Li_5Mo_2S_4$).[29,32,42,45] The subsequent CV profiles of the IE-MoS_2/MWCNTs are consistent, showing the disappearance of the two peaks at 0.99 and 0.45 V that are observed in the first cathodic scan. Instead, two pairs of redox peaks show up: the reduction peak at 1.96 V corresponds to the reverse process of the oxidation peak at 2.29 V, highlighting the redox reaction between MoS_2 and $LiMo_2S_2$ (the shallow insertion intermediate). The reduction peak at 1.23 V corresponds to the reverse process of the oxidation peak at 1.73 V, denoting the reduction/oxidation between the chemical conversion intermediates (*e.g.*, $Li_3Mo_2S_4$ and $Li_5Mo_2O_4$) and the shallow insertion intermediate ($LiMo_2S_2$). The high consistency in the CV profiles indicates good anode stability and electrochemical reversibility of the synthesized IE-MoS_2/MWCNTs. According to the density-functional theory (DFT) simulations, George *et al.* suggested the stable intermediates in the lithiation process including $LiMo_2S_2$ (shallow insertion of Li^+), $Li_3Mo_2S_4$ and $Li_5Mo_2O_4$ (intermediate insertion of Li^+ and chemical conversion), and Li_3MoS_2 with possible Li_2S, Mo atomic chains, and MoLi alloy (deep insertion and chemical conversion).[45] The lithium intercalation and conversion reaction increases the interlayer gap, while the integrity of the layered structure still remains. The calculation results indicate that the expanded interlayer spacing of MoS_2 in the synthesized IE-MoS_2/MWCNT material benefits the lithium intercalation and conversion reaction yet eliminates the structural failure of the layered MoS_2 structure.

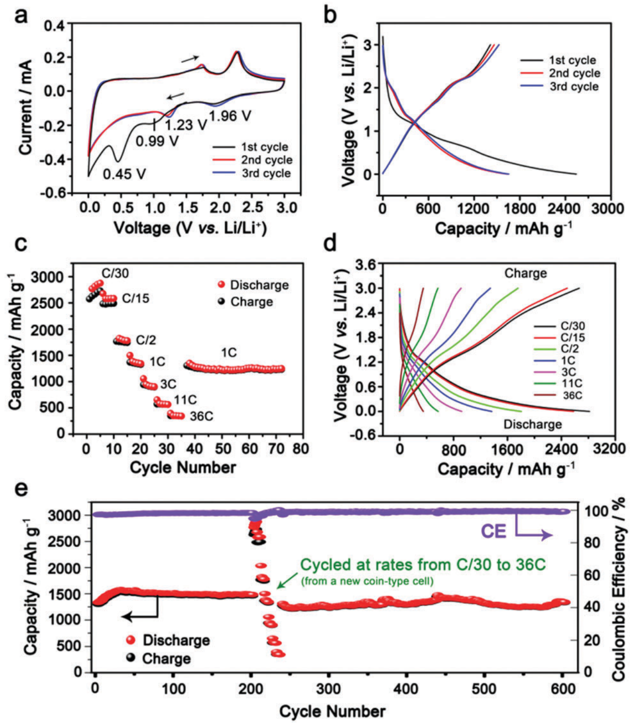

Fig. 3 Electrochemical performance of the IE-MoS_2/MWCNT anodes in lithium-ion batteries. (a) *CV* measurement of the IE-MoS_2/MWCNTs for the first 3 cycles (*i.e.*, the initial activation step). The sweep rate was 0.5 mV s^{-1} in a voltage range of 0–3 V *versus* Li/Li^+. (b) Discharge–charge voltage profiles recorded in the first three cycles with the 1C rate. (c) Comparison of discharge/charge capacities of the IE-MoS_2/MWCNT anode at various current rates from C/30 to 36C. The measurements were performed after the initial activation step. (d) Representative discharge–charge voltage profiles at various C rates. (e) Discharge/charge capacities and the corresponding coulombic efficiency measured over 600 cycles in the 0.0005–3 V range.

Comparative CV studies on pure IE-MoS_2 and MWCNTs show significant electrochemical differences from the IE-MoS_2/MWCNTs (Fig. S4 and S5, ESI†), strongly suggesting that the synergistic effect between IE-MoS_2 and MWCNTs may enable unique battery performance. Fig. 3b compares the voltage profiles of the IE-MoS_2/MWCNTs at the initial cycles. For the first cycle, the IE-MoS_2/MWCNT anode exhibits an impressive specific discharge capacity of 2538 mA h g^{-1} while the specific charge capacity drops to 1414 mA h g^{-1}, which results in a low coulombic efficiency of ∼56%. The coulombic efficiency can rapidly reach 92% in the third cycle with the discharge and charge capacities of 1655 and 1524 mA h g^{-1}, respectively. The difference in the CVs between the first scan and the following scans is consistent with the difference in the discharge curves between the first cycle and the second cycle, indicating that the initial reduction/discharge of the as-synthesized IE-MoS_2/MWCNTs involves many side reactions such as reaction with solvent molecules adsorbed on the surfaces and trapped in the interlayer gaps, adsorbed high-oxidation-state species, and possible crystalline defects. The consistency of the profiles of CVs and charge/discharge curves in the 2nd and higher cycles implies that the initial cycle conditions the electrode materials to behave reversibly in electrochemical redox processes relying on the characteristic structure and properties of the IE-MoS_2/MWCNTs (*e.g.*, enlarged interlayer gap).

The rate capability of the IE-MoS_2/MWCNTs has been assessed after the initial activation process. Fig. 3c exhibits the variation of the discharge capacity from 2686 mA h g^{-1} to 390 mA h g^{-1} at a discharge/charge rate varying from C/30 (0.053 A g^{-1}) to 36C (57.312 A g^{-1}). Furthermore, the capacity of 1442 mA h g^{-1} delivered at 1C (1.592 A g^{-1}) can be recovered and remains stable for numerous cycles after fast-rate operation (Fig. 3c). At a super high current rate of 57.312 A g^{-1} (*i.e.*, 36C), the electrode is still capable of delivering 390 mA h g^{-1} capacity in 24.5 s (Fig. 3d). Such high rate capacity value achieved for the IE-MoS_2/MWCNTs is remarkable and is far above the documented data for MoS_2-based anodes, in which rates higher than 10 A g^{-1} are barely reported.[8] Fig. 3e shows the stable capacity retention of the IE-MoS_2/MWCNTs anode upon cycling at 1C (1.592 A g^{-1}). An increase of the capacity observed in the initial 35 cycles is presumably caused by the delayed wetting of the electrolyte into the composite electrode. After the conditioning, it demonstrates a capacity of 1442 mA h g^{-1} with a coulombic efficiency of 98.4% and for a life extending 600 cycles with only 6.2% capacity decay (Fig. 3e). The battery performance of the IE-MoS_2/MWCNTs is superior to that of pure IE-MoS_2 and MWCNTs (Fig. S6 and S7, ESI†), and also outperforms the reported MoS_2-based anode materials.

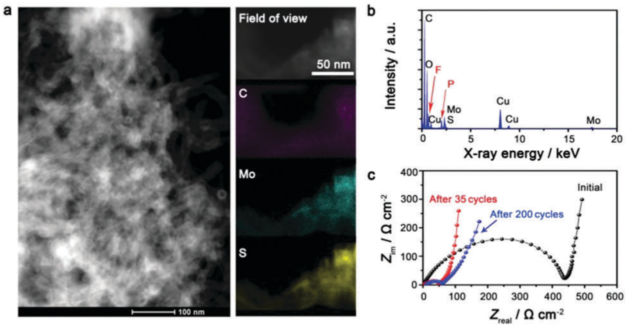

Fig. 4 Characterization of the IE-MoS_2/MWCNT electrode after discharge/charge cycles. (a) HAADF-STEM image (left) and elemental mapping (right) of the IE-MoS_2/MWCNT electrode after 200 cycles. (b) EDX spectrum of the IE-MoS_2/MWCNT electrode after 200 cycles. (c) Impedance measurements of the IE-MoS_2/MWCNT electrode before (black) and after different numbers of cycles.

The electrode after being deeply cycled has been studied to gain insight into the excellent battery performance of the IE-MoS_2/MWCNTs. The high-angle annular dark field scanning transmission electron microscopy (HAADF-STEM) image (Fig. 4a, left) reveals that the IE-MoS_2/MWCNT hybrid structures still well remain after 200 fatigue cycles but with some extent of aggregation, which is likely due to the mixing with binders in the electrode preparation process. EDX elemental mapping over a typical area of the cycled electrode shows that the spatial distributions of Mo and S are completely the same while they are different from that of C (Fig. 4a, right), implying the high possibility that Mo and S atoms still bond together after cycling. The quantitative analysis of the corresponding EDX spectrum (Fig. 4b) reveals that the atomic ratio of Mo/S is ∼1 : 2, close to the stoichiometry of MoS_2. The high-fidelity retention of spatial overlapping and stoichiometry of the Mo and S elements highlights that the long-time (200 cycles) discharge/charge operation does not completely break the original layered geometry of MoS_2 to form segregated nanoparticles. The structural integrity and interlayer distance of the cycled sample can be further studied with TEM and XRD if an appropriate method is developed to prepare a clean sample to avoid the interferences of the electrolyte and the binder.[36] The strong signal of the C element is also observed, indicating the good retention ability on electrode constituents. The F and P signals are caused by the residual $LiPF_6$ electrolyte in the vicinity of the studied electrode material. The impedance change of the IE-MoS_2/MWCNT electrode has been tracked before cycling and after 35 and 200 cycles. As shown in Fig. 4c, a tremendous impedance decrease can be observed for the cell after 35 cycles, which is attributed to the slow wetting of the electrolyte into the IE-MoS_2/MWCNTs, and also to the exclusion of foreign adsorbates and crystalline defects in the initial discharge process. The decreased impedance agrees well with the capacity increase over the first 35 cycles, as observed in Fig. 3e. No significant impedance increase is observed after 200 cycles, indicative of the limited growth of the solid electrolyte interphase during aging,[46] which further confirms the good cycling stability of the IE-MoS_2/MWCNTs.

3.3 Mechanism for high rate capability

Theoretically, the specific capacity of MoS_2 is calculated to be ∼670 mA h g^{-1} while the value for the MWCNTs is ∼340 mA h g^{-1}.[23,30,41] The measured superior capacity of the IE-MoS2/MWCNTs is strongly indicative that a favorable synergistic effect exists in this composite electrode and thus affords capacity gain. Similar improved capacities have also been reported for other nanostructured MoS_2-based composites, for example, MoS_2 decorated carbon nanofibers,[32] MoS_2/polyaniline nanowires,[42] MoS_2/MoC/carbon nanotubes,[30] MoS_2/graphene[29] and others. However, for the existing MoS_2-based materials, there is rare published data available for a rate higher than 10 A g^{-1} (Fig. 5a), and the cycling stabilities are usually demonstrated below 200 cycles. Compared with the reported electrochemical

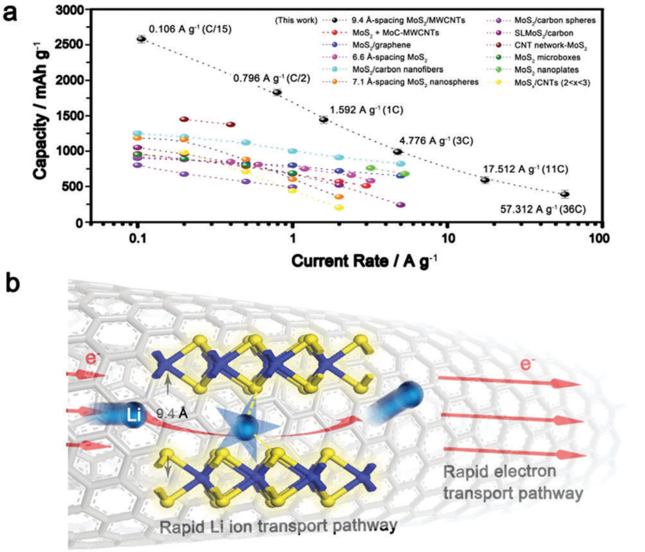

Fig. 5 (a) Comparison of rate capability for various MoS_2-based electrodes, including MoS_2 + MoC-MWCNTs,[30] MoS_2/graphene,[29] 6.6 Å-spacing MoS_2,[10] MoS_2/carbon nanofibers,[32] 7.1 Å-spacing MoS_2 nanospheres,[57] MoS_2/carbon spheres,[58] single layer MoS_2/carbon,[59] CNT network-MoS2,[60] MoS_2 microboxes,[27] MoS_2 nanoplates,[8] and MoS_x/CNTs ($2 < x < 3$).[61] (b) Schematic of the plausible mechanism responsible for the enhanced rate performance of the synthesized IE-MoS_2/MWCNTs.

data for the MoS_2-based material (Fig. 5a), our IE-MoS_2/MWCNTs offer a capacity of 390 mA h g^{-1} at a very high rate of 57.3 A g^{-1} (36C), while capacity loss is barely observed in the course of continuous charge/discharge cycles (Fig. 3c), which represents the highest rate capability of the MoS_2-based materials.

The substantially improved battery performance in terms of the high rate capability and capacity can be attributed to the highly conductive MWCNTs, the advantageous interlayer-expanded MoS_2 structure, and the synergistic effect between them, which allow for enhancing the ion and electron transport kinetics in the battery. Carbon nanotubes permit nanoscale electrical wiring of active materials to their surfaces due to the striking percolation networks,[47,48] creating good composite electrode materials with a high surface area and excellent electric conductivity. The high rate behavior is significantly benefited from the interlayer expansion of MoS_2 grafted on the MWCNTs. As for the layered materials, the insertion and transport of lithium ions is mainly determined by the diffusion energy barrier formed between a polarizing cation and a negatively charged host lattice.[5,49] For example, bulk MoS_2 with an interlayer spacing of 6.2 Å exhibits a calculated diffusion barrier of $\sim$0.49 eV.[4] Recent studies suggest that such slow kinetics can be circumvented by enlarging the interlayer spacing of MoS_2,[8,24,50] or by reducing dimensionality to the monolayer,[4] thus facilitating the insertion and diffusion of lithium ions. Despite these successes, MoS_2-based materials performing at high current rates are rarely demonstrated, owing to the lack of effective approaches to further expand the interlayer spacing that permits an optimized lithium–MoS_2 interaction (reported values are often $<$6.9 Å).[8,10,24,51–55] Fig. 5b highlights how the high electrical conductivity of the MWCNTs and the expanded interlayer spacing of the MoS_2 nanosheets cooperate to enable the fast lithium intercalation/diffusion and the following redox reaction involving electron transfer. The significantly expanded interlayer spacing (9.4 Å) facilities the insertion of lithium into the interlayer gaps in the grafted MoS_2 nanosheets as well as the following lithium diffusion in the interlayer gaps.[56] Once lithium diffuses to the appropriate sites, the redox reaction can occur between lithium and MoS_2 and the involving electrons can quickly migrate through the individual S–Mo–S layers to the MoS_2 edges interfaced with the MWCNTs, which efficiently guide the electrons to the collecting electrode. Due to the large interlayer gaps that allow all the MoS_2 units to (fully) wet with the lithium ions, the molecular layer structure can be maintained even after the IE-MoS_2/MWCNTs undergo a deep chemical conversion. In contrast, deep chemical conversion breaks the molecular layers of MoS_2 to enable the lithium ions to diffuse to the buried MoS_2 units of the MoS_2 nanosheets with narrow interlayer gaps. The unique features of the synthesized IE-MoS_2/MWCNTs enable outstanding rate capability that outperforms almost all the reported counterpart MoS_2-based electrode materials.

4. Conclusion

In summary, we have demonstrated a high-performance anode material composed of MoS_2 nanosheets with significantly expanded interlayer spacing, which are directionally assembled around highly percolated MWCNTs to exhibit very short lithium diffusion lengths as well as efficient and rapid pathways for electron and ion transport, boosting discharge/charge kinetics. This newly developed composite material displays remarkable capability at a high current rate even up to 57.3 A g^{-1} (36C) and is also very stable for over 600 cycles, representing the first MoS_2-based material attempting towards high-rate charge and discharge use. These understandings shed light on the rational design of high-performance anode materials with superior rate capability that can be achieved by controlling the nucleation and growth kinetics of colloidal chemistry. The IE-MoS_2/MWCNT hybrid structures exhibit major features completely different from the widely studied MoS_2/rGO (reduced graphene oxide) composites.[62–64] The MoS_2/rGO composites usually form layer-by-layer stacking structures with the small-sized MoS_2 layers embedded in the stacked rGO sheets, resulting in a difficulty in exposing the MoS_2 edges to the electrolyte in batteries. Since the intercalation/deintercalation of ions in MoS_2 is dominated by the diffusion of ions through the MoS_2 edges into/out of the MoS_2 interlayer gaps, embedding the MoS_2 in stacked rGO dramatically reduces the diffusion rate of ions (*i.e.*, lower rate capability of the corresponding batteries). In contrast, the IE-MoS_2/MWCNT composite (Fig. 2) completely eliminates the disadvantages of the MoS_2/rGO composites. The IE-MoS_2 nanosheets extend out of the MWCNTs to fully expose the MoS_2 edges to the electrolyte, facilitating the intercalation/deintercalation of ions in the MoS_2 interlayer gaps and thus improving the rate capability of the corresponding batteries. The unique geometry of the IE-MoS_2/MWCNT structure and the expanded interlayer spacing of

IE-MoS_2 can also benefit the high electrical conductivity in individual S–Mo–S molecular layers, through which the electrons can quickly transfer to the highly conductive MWCNTs, to lower the impedance of the corresponding anodes. It is worthy to note that the high surface area of the nanostructured IE-MoS_2/MWCNT electrode materials may induce a non-negligible capacitive behaviour to make a contribution to the electrochemical energy storage capacity of the materials. The actual contribution of storage capacity associated with the lithium intercalation and conversion reaction may be smaller than the measured capacity (Fig. S8, ESI†).

Conflicts of interest

There are no conflicts to declare.

Acknowledgements

Use of the Center for Nanoscale Materials and the Advanced Photon Source (APS) was supported by the U.S. Department of Energy, Office of Science, Office of Basic Energy Sciences, under Contract No. DE-AC02-06CH11357.

Notes and references

1 M. Armand and J. M. Tarascon, *Nature*, 2008, **451**, 652.
2 B. Kang and G. Ceder, *Nature*, 2009, **458**, 190.
3 H. Zhang, X. Yu and P. V. Braun, *Nat. Nanotechnol.*, 2011, **6**, 277.
4 Y. Li, D. Wu, Z. Zhou, C. R. Cabrera and Z. Chen, *J. Phys. Chem. Lett.*, 2012, **3**, 2221–2227.
5 Y. Liang, H. D. Yoo, Y. Li, J. Shuai, H. A. Calderon, F. C. Robles Hernandez, L. C. Grabow and Y. Yao, *Nano Lett.*, 2015, **15**, 2194–2202.
6 S. Yang, D. Li, T. Zhang, Z. Tao and J. Chen, *J. Phys. Chem. C*, 2012, **116**, 1307–1312.
7 Z. Hu, L. Wang, K. Zhang, J. Wang, F. Cheng, Z. Tao and J. Chen, *Angew. Chem.*, 2014, **126**, 13008–13012.
8 H. Hwang, H. Kim and J. Cho, *Nano Lett.*, 2011, **11**, 4826–4830.
9 Y. Li, Y. Liang, F. C. Robles Hernandez, H. Deog Yoo, Q. An and Y. Yao, *Nano Energy*, 2015, **15**, 453–461.
10 H. Liu, D. Su, R. Zhou, B. Sun, G. Wang and S. Z. Qiao, *Adv. Energy Mater.*, 2012, **2**, 970–975.
11 M. Chhowalla, H. S. Shin, G. Eda, L.-J. Li, K. P. Loh and H. Zhang, *Nat. Chem.*, 2013, **5**, 263.
12 Q. H. Wang, K. Kalantar-Zadeh, A. Kis, J. N. Coleman and M. S. Strano, *Nat. Nanotechnol.*, 2012, **7**, 699.
13 K. Cao, T. Jin, L. Yang and L. Jiao, *Mater. Chem. Front.*, 2017, **1**, 2213–2242.
14 M. Hafeez, L. Gan, A. Saleem Bhatti and T. Zhai, *Mater. Chem. Front.*, 2017, **1**, 1917–1932.
15 G. Zhang, H. Liu, J. Qu and J. Li, *Energy Environ. Sci.*, 2016, **9**, 1190–1209.
16 J. Wang, H. Tang, L. Zhang, H. Ren, R. Yu, Q. Jin, J. Qi, D. Mao, M. Yang, Y. Wang, P. Liu, Y. Zhang, Y. Wen, L. Gu, G. Ma, Z. Su, Z. Tang, H. Zhao and D. Wang, *Nat. Energy*, 2016, **1**, 16072.
17 J. Wang, N. Yang, H. Tang, Z. Dong, Q. Jin, M. Yang, D. Kisailus, H. Zhao, Z. Tang and D. Wang, *Angew. Chem., Int. Ed.*, 2013, **52**, 6417–6420.
18 J. Kibsgaard, Z. Chen, B. N. Reinecke and T. F. Jaramillo, *Nat. Mater.*, 2012, **11**, 963.
19 Y. Huang, J. Guo, Y. Kang, Y. Ai and C. M. Li, *Nanoscale*, 2015, **7**, 19358–19376.
20 Y. Hu, Y. Huang, C. Tan, X. Zhang, Q. Lu, M. Sindoro, X. Huang, W. Huang, L. Wang and H. Zhang, *Mater. Chem. Front.*, 2017, **1**, 24–36.
21 B. Radisavljevic, A. Radenovic, J. Brivio, V. Giacometti and A. Kis, *Nat. Nanotechnol.*, 2011, **6**, 147.
22 O. Lopez-Sanchez, D. Lembke, M. Kayci, A. Radenovic and A. Kis, *Nat. Nanotechnol.*, 2013, **8**, 497.
23 T. Stephenson, Z. Li, B. Olsen and D. Mitlin, *Energy Environ. Sci.*, 2014, **7**, 209–231.
24 G. Du, Z. Guo, S. Wang, R. Zeng, Z. Chen and H. Liu, *Chem. Commun.*, 2010, **46**, 1106–1108.
25 M.-R. Gao, Y.-F. Xu, J. Jiang and S.-H. Yu, *Chem. Soc. Rev.*, 2013, **42**, 2986–3017.
26 D. K. Nandi, U. K. Sen, D. Choudhury, S. Mitra and S. K. Sarkar, *Electrochim. Acta*, 2014, **146**, 706–713.
27 L. Zhang, H. B. Wu, Y. Yan, X. Wang and X. W. Lou, *Energy Environ. Sci.*, 2014, **7**, 3302–3306.
28 J. Wang, H. Tang, H. Wang, R. Yu and D. Wang, *Mater. Chem. Front.*, 2017, **1**, 414–430.
29 K. Chang and W. Chen, *ACS Nano*, 2011, **5**, 4720–4728.
30 X. Li, J. Zhang, R. Wang, H. Huang, C. Xie, Z. Li, J. Li and C. Niu, *Nano Lett.*, 2015, **15**, 5268–5272.
31 J.-Z. Wang, L. Lu, M. Lotya, J. N. Coleman, S.-L. Chou, H.-K. Liu, A. I. Minett and J. Chen, *Adv. Energy Mater.*, 2013, **3**, 798–805.
32 F. Zhou, S. Xin, H.-W. Liang, L.-T. Song and S.-H. Yu, *Angew. Chem., Int. Ed.*, 2014, **53**, 11552–11556.
33 A. Saha, A. Mondal, S. Maiti, S. C. Ghosh, S. Mahanty and A. B. Panda, *Mater. Chem. Front.*, 2017, **1**, 1585–1593.
34 J. Xiao, D. Choi, L. Cosimbescu, P. Koech, J. Liu and J. P. Lemmon, *Chem. Mater.*, 2010, **22**, 4522–4524.
35 V. Datsyuk, M. Kalyva, K. Papagelis, J. Parthenios, D. Tasis, A. Siokou, I. Kallitsis and C. Galiotis, *Carbon*, 2008, **46**, 833–840.
36 G. Jia, D. Chao, N. H. Tiep, Z. Zhang and H. J. Fan, *J. Mater. Chem. A*, 2018, **14**, 136–142.
37 Y. Sun, F. Alimohammadi, D. Zhang and G. Guo, *Nano Lett.*, 2017, **17**, 1963–1969.
38 M.-R. Gao, M. K. Y. Chan and Y. Sun, *Nat. Commun.*, 2015, **6**, 7493.
39 M. Endo, K. Takeuchi, T. Hiraoka, T. Furuta, T. Kasai, X. Sun, C. H. Kiang and M. S. Dresselhaus, *J. Phys. Chem. Solids*, 1997, **58**, 1707–1712.
40 Y. Sun, L. Wang, Y. Liu and Y. Ren, *Small*, 2015, **11**, 300–305.
41 M. A. Py and R. R. Haering, *Can. J. Phys.*, 1983, **61**, 76–84.
42 L. Yang, S. Wang, J. Mao, J. Deng, Q. Gao, Y. Tang and O. G. Schmidt, *Adv. Mater.*, 2013, **25**, 1180–1184.
43 G. X. Wang, S. Bewlay, J. Yao, H. K. Liu and S. X. Dou, *Electrochem. Solid-State Lett.*, 2004, **7**, A321–A323.

44 J. Xiao, X. Wang, X.-Q. Yang, S. Xun, G. Liu, P. K. Koech, J. Liu and J. P. Lemmon, *Adv. Funct. Mater.*, 2011, **21**, 2840–2846.

45 C. George, A. J. Morris, M. H. Modarres and M. De Volder, *Chem. Mater.*, 2016, **28**, 7304–7310.

46 H. Wu, G. Yu, L. Pan, N. Liu, M. T. McDowell, Z. Bao and Y. Cui, *Nat. Commun.*, 2013, **4**, 1943.

47 Y. J. Lee, H. Yi, W.-J. Kim, K. Kang, D. S. Yun, M. S. Strano, G. Ceder and A. M. Belcher, *Science*, 2009, **324**, 1051.

48 J. S. Sakamoto and B. Dunn, *J. Electrochem. Soc.*, 2002, **149**, A26–A30.

49 G. G. Amatucci, F. Badway, A. Singhal, B. Beaudoin, G. Skandan, T. Bowmer, I. Plitz, N. Pereira, T. Chapman and R. Jaworski, *J. Electrochem. Soc.*, 2001, **148**, A940–A950.

50 C. Feng, J. Ma, H. Li, R. Zeng, Z. Guo and H. Liu, *Mater. Res. Bull.*, 2009, **44**, 1811–1815.

51 M. Choi, S. K. Koppala, D. Yoon, J. Hwang, S. M. Kim and J. Kim, *J. Power Sources*, 2016, **309**, 202–211.

52 G. Qu, J. Cheng, Z. Wang, B. Wang and S. Ye, *J. Mater. Sci.*, 2016, **51**, 4739–4747.

53 K. D. Rasamani, F. Alimohammadi and Y. Sun, *Mater. Today*, 2017, **20**, 83–91.

54 M. Wang, G. Li, H. Xu, Y. Qian and J. Yang, *ACS Appl. Mater. Interfaces*, 2013, **5**, 1003–1008.

55 Y. Xia, B. Wang, X. Zhao, G. Wang and H. Wang, *Electrochim. Acta*, 2016, **187**, 55–64.

56 Y. Ji, Q. Wei and Y. Sun, *Ind. Eng. Chem. Res.*, 2018, **57**, 4571–4576.

57 S. Zhang, B. V. R. Chowdari, Z. Wen, J. Jin and J. Yang, *ACS Nano*, 2015, **9**, 12464–12472.

58 L. Zhang and X. W. Lou, *Chem. – Eur. J.*, 2014, **20**, 5219–5223.

59 C. Zhao, J. Kong, L. Yang, X. Yao, S. L. Phua and X. Lu, *Chem. Commun.*, 2014, **50**, 9672–9675.

60 H. Wang, Z. Lu, D. Kong, J. Sun, T. M. Hymel and Y. Cui, *ACS Nano*, 2014, **8**, 4940–4947.

61 Y. Shi, Y. Wang, J. I. Wong, A. Y. S. Tan, C.-L. Hsu, L.-J. Li, Y.-C. Lu and H. Y. Yang, *Sci. Rep.*, 2013, **3**, 2169.

62 L. David, R. Bhandavat and G. Singh, *ACS Nano*, 2014, **8**, 1759–1770.

63 Y. Liu, Y. Zhao, L. Jiao and J. Chen, *J. Mater. Chem. A*, 2014, **2**, 13109–13115.

64 X. Xie, Z. Ao, D. Su, J. Zhang and G. Wang, *Adv. Funct. Mater.*, 2015, **25**, 1393–1403.